

## MOTION RESPONSE PREDICTION OF MARINE VESSELS BASED ON HYDRODYNAMIC MODELS UPDATED THROUGH ON-SITE MEASUREMENTS

Gowtham Radhakrishnan<sup>1,2</sup>, Bernt J. Leira<sup>1,2</sup>, Zhen Gao<sup>1,2</sup>, Svein Sævik<sup>1,2</sup>, Alojz Gomola<sup>1</sup>

Department of Marine Technology<sup>1</sup>

Centre for Marine Operations in Virtual Environments (SFI MOVE)<sup>2</sup>

Norwegian University of Science and Technology

Trondheim, Norway

### ABSTRACT

Decision support systems in offshore vessels utilize wave parameters in combination with physics-based vessel models to predict the vessel behavior prior to the initiation and execution of a marine operation. These predictions are, usually, accompanied by significant uncertainties inherent in the estimation of wave statistical parameters, idealized parametric spectra, and system variables. Consequently, the predictions may deviate considerably from the real behavior of the vessel. Therefore, this study uses numerical wave spectra corresponding to a site in the North Sea in conjunction with a hydrodynamic model adapted to measurements to make more accurate intermediate-term response predictions. Considering a weather-restricted marine operation, the intermediate-term predictions involve simulating the responses for any time window within the upcoming 72 hours. The vessel model's uncertainty is minimized by calibrating the influential parameters utilizing the full-scale response measurements within an optimization framework. The subsequent Roll predictions based on calibrated parameters exhibit better alignment with the measured Roll motions. The application of recursive optimization showed a significant reduction in prediction errors in an actual marine operation.

**Keywords:** Decision support systems, intermediate-term predictions, numerical wave spectra, calibrated hydrodynamic model

### NOMENCLATURE

ECMWF	European Center for Medium-Range Weather Forecasts
FD	Frequency Domain
FFT	Fast Fourier Transform
HFM	High-fidelity model

LFM	Low-fidelity model
JONSWAP	Joint North Sea Wave Project
MADS	Mesh Adaptive Direct Search
NDBC	National Data Buoy Center
PCE	Polynomial Chaos Expansion
QoI	Quantity of Interest
WAM	Wind-Wave model
$M$	Vessel mass
$I_{44}$	Roll moment of inertia
$I_{55}$	Pitch moment of inertia
$I_{66}$	Yaw moment of inertia
$\beta_{33}$	Additional linearized Heave damping coefficient
$\beta_{44}$	Additional linearized Roll damping coefficient
$\beta_{55}$	Additional linearized Pitch damping coefficient
$\beta_{33,cr}$	Critical Heave damping coefficient
$\beta_{44,cr}$	Critical Roll damping coefficient
$\beta_{55,cr}$	Critical Pitch damping coefficient
CoG	Center of Gravity
$x_{cg}$	Longitudinal coordinate of CoG
$y_{cg}$	Transverse coordinate of CoG
$z_{cg}$	Vertical coordinate of CoG

### 1. INTRODUCTION

The safe execution of any marine operation is a challenging task in the presence of harsh ocean conditions. Proper planning prior to the operation is crucial for decision making, thereby saving considerable costs and human efforts. Decision support systems onboard a vessel can greatly aid the vessel operators in performing planned actions. Customarily, the vessel owners plan the execution of an operation by deducing the operational limits based on the environmental conditions [1] [2]. The point often stressed is that the

operational limits derived based on the vessel responses can be more dependable than those based on the environmental conditions [3] [4]. The former is called the response-based decision-making methodology. This study mainly focuses on reducing the uncertainties associated with the response-based decision-making methodology; thus, the resulting vessel responses predictions can closely mimic the actual vessel's behavior. The uncertainties originate from the idealizations in the parametric spectra, ocean wave modeling, and hydrodynamic system parameters. Of these, the measures to eliminate the uncertainties arising from the parametric spectra and vessel system properties are addressed in this work.

The wave information issued from the weather-service providers is utilized for making intermediate-term predictions. The prediction of vessel responses for any time window within the upcoming 72 hours comes under the intermediate-term response prediction category. The traditional approach is to procure sea state parameters like significant wave height, peak period, and mean wave direction of wind sea and swell. Followingly, the parametric wave spectra such as the JONSWAP, Pierson-Moskowitz, Ochi-Hubble spectrum can be constructed by applying the wave parameters [5]. Moreover, directional nature can be imparted to these 1-dimensional spectra using formulations involving cosine-spreading functions [6]. However, such 2-dimensional parametric spectra provide only an idealized energy spread of ocean waves, and their application is site-dependent. Due to such shortcomings, they may not reflect the exact energy distribution of ocean waves at our location of interest. On the contrary, the numerical spectra offer complete information on the energy spread of the wind sea and different partitions of swell at any geographic location. Thus, the wave energy spread can be obtained at a high resolution than what usually is available from parametric spectra. Therefore, the numerical wave spectra issued by weather-service providers have been utilized in this work. The numerical spectra are directly obtained from the third-generation wave models. The wave models are based on solving the balance equation of the wave energy or wave action density. For instance, the Wind-Wave (WAM) model is based on the energy balance equation [7], while the Wave Watch III model uses the action balance equation [8].

The ocean wave parameters can also be measured at a site using moored buoys or remotely from space using Altimetry Satellites and Synthetic Aperture Radars. Mostly, the weather service providers calibrate the numerical weather models using the wave observations from satellites. As a supplement the buoy data is, predominantly, employed for validating the satellite data and numerical models.

Besides the uncertainties in parametric spectra, the Frequency Domain (FD) simulations also suffer from uncertainties related to the hydrodynamic system parameters. These parameters assume random values and thereby contribute to significant variations in vessel rigid body responses during a marine operation. Some of these parameters depend on the vessel

operational conditions, whereas the other variables change with the sea states. However, not all these parameters influence the vessel responses to a considerable extent. Only a few variables are essential for each rigid body response, and it is considered vital to update them during the operation. The influential variables can be identified by performing a complete probabilistic sensitivity study. The variance-based Sobol' indices are highly useful in quantitatively identifying the effects of input uncertainties on the output response. Especially, it is remarkably cost-effective when such indices are computed using Polynomial Chaos Expansion(PCE). Sudret [9], Blatman [10], Deman et al. [11], Mai [12], have applied the PCE-Sobol' indices in the uncertainty analysis of problems associated with the engineering disciplines such as structural, hydrogeology, and earthquake engineering. Radhakrishnan et al. [13] studied the uncertainty effects of input parameters on the vessel's rigid body response Root Mean Square (RMS). Based on the sensitivity study, the highly influential variables are chosen and subjected to calibration using measured responses. Some previous studies have tuned certain essential parameters of an offshore vessel model using response measurements from lab experiments. For instance, Han et al. [14] employed an unscented Kalman filtering technique to update the  $Z_{cg}$ , inertia, and damping parameters. Kaasen et al. [15] applied a gradient-based optimization approach to tune the mass and stiffness matrices. Skandeli [16] used the Golden Section method to update the parameters of a semi-submersible. This study aims to calibrate the numerical model of an offshore vessel by utilizing the full-scale measurements of the actual asset. A derivative-free optimization procedure applicable for non-linear functions is applied to minimize the error between the simulated and measured responses, and determine the optimal influential parameters.

The paper is organized as follows. In Section 2, a case study of an actual marine operation is introduced. Further, relevant theoretical descriptions and practical implementation of the methods associated with the model calibration framework are presented. Section 3 presents the sensitivity study, calibration analysis, and validation of results. Finally, conclusive points are provided in Section 4.

## 2. THEORY AND METHODOLOGY

### 2.1 Case Study

The methodology considers a real case study involving an offshore vessel named Olympic Challenger. As shown in Figure 1, the vessel's operational site was at a location in the North sea, and it was performing a weather-limited crane operation. The date, exact location, and other details related to the nature of the operation are not mentioned here due to confidentiality issues. The vessel motions are measured using the SeaPath 200 Inertial Measurement Unit (IMU). These measured responses were utilized for model calibration and subsequent validation.

The hydrodynamic calculations were performed in Wamit 7 by

applying a representative panel model shown in Figure 1. The relevant dimensions of the numerical model are provided in Table 1. The positive  $X$ -axis ( $x = 0$ ) is at  $Lpp/2$ , the positive  $Y$ -axis is towards the port side, and the positive  $Z$ -axis is pointing upwards with  $z = 0$  in the still water plane.

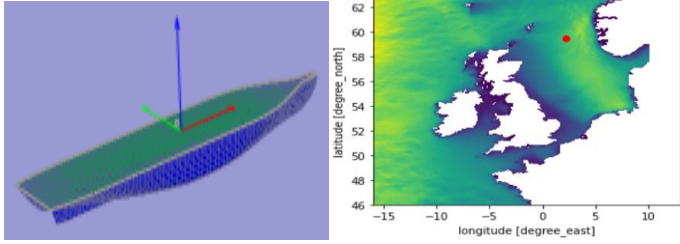


Figure 1 Left: Numerical panel model of the Olympic Challenger applied for Wamit calculations. Right: Geographical position of the actual vessel shown using a red-pointer.

Table 1 Dimensions of the numerical model

Overall Length, $LOA$	105.9 m
Length between perpendiculars, $Lpp$	94.7 m
Breadth, $B$	21 m
Draught, $T$	6.28 m
Volume	8999 $m^3$
Waterplane Area	1842 $m^2$
Total no. of panels	3232

## 2.2 Wave Spectra

The wave conditions at the relevant site were represented through a 2-dimensional numerical wave spectrum in the Frequency domain response analysis. The numerical wave spectrum was simulated using the WAM model utilizing the wind-forcing inputs from ECMWF ERA5 [16]. ERA5 denotes a metocean database consisting of reanalysis of environmental conditions such as waves, winds [16].

The wave directions in the ECMWF spectra follow the Oceanographic axis conventions. The reference  $0^\circ$  is at South, and the increase in directions is as per the clock-wise rule. In other words,  $0^\circ$  denotes the waves propagating from the South. However, the mean wave direction parameter ( $\theta_m$ ) in the ERA5 database follows the meteorological conventions, i.e., defined clock-wise from the reference North.  $\theta_m$  is converted to the Oceanographic conventions by deducting with  $180^\circ$ . Finally, the relative wave direction ( $\theta_R$ ) for vessel response analysis was calculated by

$$\theta_R = V_\theta - (\theta_m - 180) \quad (1)$$

where  $V_\theta$  is the vessel heading. The 2-dimensional wave spectra from ECMWF were constructed using 30 frequencies and 24 wave directions. To comply with the directions and

frequencies used in the computation of transfer functions, the numerical spectra were extended to 72 wave directions and 152 wave frequencies by applying linear interpolation. The ERA5 database provides directional spectra for the total sea shown in Figure 2 a). In Figure 2 b) and c), the total sea spectrum was split into wind-wave and swell spectra using the formulation proposed by Komen et al. [17]. The wind-wave spectrum is usually single modal since local winds drive them specifically. However, the swells are caused by distant storms; therefore, the swell spectrum has different systems and is multimodal in nature.

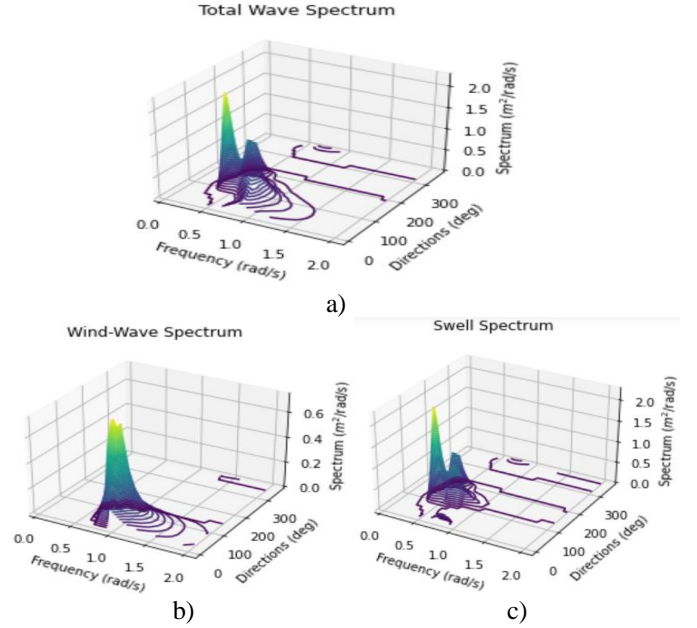


Figure 2 a) Complete 2-dimensional numeric wave spectrum representing the total sea in the North Sea region on March 19 2020 00:00 UTC. b) The spectrum is split into b) wind-wave and c) swell spectrum using the formulation proposed by Komen et al. [17].

## 2.3 Hydrodynamic Analysis

The complex-valued motion transfer function,  $\overline{T}_{\zeta Z} \in \mathbb{C}^{q \times 1}$ , relates the wave elevation  $\zeta$  at a reference point to the motion response  $\vec{Z} = \{(Z_q), q=1,2,\dots,6\}$ . The index notation  $q$  is used for expressing the six DoFs of vessel motions (Surge, Sway, Heave, Roll, Pitch, Yaw).

The motion transfer function ( $\overline{T}_{\zeta Z}$ ) is a product of the transfer function ( $\overline{T}_{FZ} \in \mathbb{C}^{q \times q}$ ) between the wave excitation loads and the motion response and the wave excitation transfer function ( $\overline{T}_{\zeta F} \in \mathbb{C}^{q \times 1}$ )

$$\overline{T}_{\zeta Z}(\omega, \theta; \mathbf{x}) = \overline{T}_{FZ}(\omega; \mathbf{x}) \cdot \overline{T}_{\zeta F}(\omega, \theta) \quad (2)$$

where  $\omega$  is the wave frequency,  $\theta$  denotes the relative directions, and system variables are given by  $\mathbf{x} = \{(x_i), i = 1, 2, \dots, D\}$ .  $D$  represents the number of input variables.

The squared amplitude values of the motion transfer function,  $\left\{T_{\zeta z_q}^* T_{\zeta z_r}^* = \left|T_{\zeta z_{q,r}}\right|^2, \forall q = r, r = 1, 2, \dots, 6\right\}$ , are determined using a hydrodynamic code [18]. The real-valued auto-response spectrum ( $S_{z_{qq}}(\omega, \theta; \mathbf{x}) \in \mathbb{R}^{+\omega \times \theta}$ ) is written as

$$S_{z_{qq}}(\omega, \theta; \mathbf{x}) = S_{\zeta}(\omega, \theta) \left|T_{\zeta z_{q,r}}(\omega, \theta; \mathbf{x})\right|^2, r=q \quad (3)$$

The RMS or standard deviation of the response can be cast as

$$\sigma_{z_q}(\mathbf{x}) = \sqrt{\sum_{h=1}^{N_{\omega}} S_{z_{qq}}(\omega_h, \mathbf{x}) \Delta \omega} \quad (4)$$

$N_{\omega}$  is the total number of frequency components.

The simulated response spectrum ( $S_{z_{qq}}(\omega, \theta; \mathbf{x})$ ) is the primary Quantity of Interest (QoI) in the model calibration work. The Welch's Fast Fourier Transform (FFT) [19] with 'Hanning' window was applied to generate the measured response spectrum ( $S_{z_{qq,MT}}$ ) from the time series measurements. The information on the measurement noise was not available, thus, no noise removal techniques were applied to the measurements.

## 2.4 Probabilistic Sensitivity Study

The system variables are inherently uncertain in nature and consequently drive the variation of vessel responses. Thus, it is essential to identify the most important parameters influencing the vessel responses. For the variable identification, a probabilistic sensitivity study using variance-based Sobol' indices was pursued. An efficient Polynomial Chaos surrogate model was applied to replace the high-fidelity model while performing sensitivity analysis. A concise description regarding the Sobol' indices is given below. The Sobol' index results and the identified most influencing parameters are presented in Sec. 3.1 for the case study.

The stochastic response of a computational model can be written as  $Y = \mathcal{M}(\mathbf{X})$ , with  $Y$  representing the output QoIs.  $\mathbf{X} = \{X_i, i = 1, 2, \dots, D\}$ , denotes the vector of independent random variables in the physical probability space. In this section alone, the system parameters are denoted by ' $\mathbf{X}$ ', as they represent the random variables associated with a probability measure. It is assumed that  $\mathcal{M}(\mathbf{X})$  is square-integrable in the associated probability measure, has a finite variance, decomposition of  $\mathcal{M}(\mathbf{X})$  satisfies uniqueness and orthogonality properties [21].

Then, the variance is decomposed as

$$V = Var[\mathcal{M}(\mathbf{X})] = \sum_{i=1}^D V_i + \sum_{1 \leq i < j \leq D} V_{ij} + \dots + V_{1\dots D} = \sum_l V_l \quad (5)$$

Here,  $V_i = V[\mathbb{E}[\mathcal{M}(\mathbf{X})|X_i]]$ ,  $V_{ij} = V[\mathbb{E}[\mathcal{M}(\mathbf{X})|X_i, X_j]] - V_i - V_j$ .  $\mathbb{E}[\mathcal{M}(\mathbf{X})|X_i]$  and  $\mathbb{E}[\mathcal{M}(\mathbf{X})|X_i, X_j]$  represent the conditional

expectation of the response QoI with respect to each input variable  $X_i$  and any two combinations of input variables  $X_i X_j$ , respectively.  $l = \{i_1, \dots, i_s\} \subset \{1, \dots, D\}$  is a generic index set, and consequently,  $X_l$ , a sub-vector of  $\mathbf{X}$ , is composed of elements whose indices correspond to the index set  $l$ . The sensitivity of the model response is obtained by dividing the individual variance terms in Eq. (5) by the total variance. The sensitivity is given by

$$\sum_{i=1}^D SI_i + \sum_{1 \leq i < j \leq D} SI_{ij} + \dots + SI_{1\dots D} = \sum_l SI_l = 1 \quad (6)$$

$SI_i$  denotes the first-order indices that quantify the effect of each uncertain parameter on the response. The second-order indices,  $SI_{ij}$ , assess the interactions between two variables and their consequent effects on the response. Depending on the number of input variables, the Sobol' indices consist of higher-order terms related to the interactions among larger combinations of random variables, i.e., third-order, fourth-order indices, and so on. The total sensitivity is the summation of the main/first-order effects and all the interaction terms in Eq. (6). It is computationally demanding to calculate all the higher-order terms and then the total sensitivity. Therefore, the total sensitivity is calculated by a simple statistical expression in Eq. (9).  $X_{\sim i}$  represents all input variables other than  $X_i$ . The formulae for the first, second, and total-order indices are provided in Eqs. (7) – (9).

$$SI_i = \frac{V[\mathbb{E}[\mathcal{M}(\mathbf{X})|X_i]]}{V[\mathcal{M}(\mathbf{X})]} \quad (7)$$

$$SI_{ij} = \frac{V[\mathbb{E}[\mathcal{M}(\mathbf{X})|X_i, X_j]]}{V[\mathcal{M}(\mathbf{X})]} - SI_i - SI_j \quad (8)$$

$$SI_i^T = 1 - \frac{V[\mathbb{E}[\mathcal{M}(\mathbf{X})|X_{\sim i}]]}{V[\mathcal{M}(\mathbf{X})]} \quad (9)$$

Based on the works of Sudret [9], Blatman [10], the computation of Sobol' indices using PCE was performed here. The details related to the derivation of Sobol' indices from polynomial coefficients can be found in [9] [10] [11] [12]

## 2.5 Derivative-Free optimization

The model calibration minimizes the error between the simulated and the measured response spectra. The calibration was conducted as an optimization problem of the form

$$\text{minimize } f(\mathbf{x}), \forall \mathbf{x} \in \mathbb{R}^D$$

$\mathbf{x}$  is a vector denoting the variables from  $D$  dimensional space, and  $f(\mathbf{x})$  represents the objective function. Each variable  $x_i$  was confined using bounded constraints with upper and lower limits denoted by  $lo_i$  and  $up_i$ , respectively. Therefore, it resulted in a restricted search space ( $\Omega$ )

$$\Omega = \{\mathbf{x} | lo_i \leq x_i \leq up_i\} \subset \mathbb{R}^D$$

The minimization was carried out through Lipschitz optimization. Accordingly, the objective function was formulated as

$$f_{\Omega, SPEC}(\mathbf{x}) = \sum_q \left( \sum_{h=1}^{N\omega} \left| w^2 ((S_{Z_{qq}, MT}(\omega_h; \mathbf{x}) \Delta\omega)^2 - (S_{Z_{qq}}(\omega_h; \mathbf{x}) \Delta\omega)^2) \right| \right) \quad (10)$$

where  $w$  denotes the optimization weights, and  $q$  is the index of the rigid body modes as defined in Sec. 2.3. If just one mode is calibrated, the weights for the rest of the modes can be assigned with zero value. The function uses the absolute value of the squared difference due to better numerical stability. The objective function was minimized using a derivative-free, non-linear optimization technique called Mesh Adaptive Direct Search (MADS) [20]. The working principle in MADS is that the input variable space is discretized using a mesh. Simultaneously, the algorithm iteratively evaluates the objective function at different points inside the mesh. The structure of the mesh can be written as

$$M_k = \cup_{\mathbf{x}_k \in Q_k} \{\mathbf{x}_k + \Delta_k^m E b, b \in \mathbb{Z}^{+D_{dir}}\},$$

where  $Q_k$  denotes the sample points generated during the initiation of iteration  $k$ .  $\Delta_k^m$  denotes the mesh size parameter.  $E$  represents the mesh directions of size  $D \times D_{dir}$ .  $D_{dir}$  is the number of directions in each dimension  $D$ .  $b$  represents positive integer vectors of size  $D_{dir}$ . MADS follows the three steps – search, poll, and update step, at each iteration [21]. During the search step, the sampling points are generated on the mesh using Latin Hypercube (LH) sampling. Then the objective function is evaluated at these points.

The poll step is executed if the search step could not provide an improved mesh point ( $f_{\Omega}(\mathbf{x}_{k+1}) < f_{\Omega}(\mathbf{x}_k)$ ) than the current best point. The poll trial points can be represented using

$$P_k = \{\mathbf{x}_k + \Delta_k^m e; e \in E_k\} \subset M_k$$

where  $E_k$  signifies the poll directions, whose columns form a set of positive basis vectors. The outcome of the poll step dictates the mesh refinement. If there is a success ( $f_{\Omega}(\mathbf{x}_{k+1}) < f_{\Omega}(\mathbf{x}_k)$ ) during the poll step of the current iteration, the mesh size is either increased or remains the same ( $\Delta_{k+1}^m \geq \Delta_k^m$ ) for the next iteration  $k+1$ ; however, the mesh size is decreased ( $\Delta_{k+1}^m < \Delta_k^m$ ) if an iteration fails. The poll size parameter, defined at this step, is also updated,  $\Delta_k^p = \sqrt{\Delta_k^m}$ . The mesh refinement concept is illustrated in Figure 3. Thin black lines, spaced at  $\Delta_k^m$  from each other, denote the mesh discretization. The poll trial points  $P_k$  are present on the thick blue frame at a distance of  $\Delta_k^p$  from the current point  $\mathbf{x}_k$ . The optimization can be terminated using any of the stopping criteria such as the maximum number of function evaluations, maximum number

of iterations, or minimum function value [22].

There are two types of MADS – LTMADS and OrthoMADS based on the generated poll directions  $E_k$ . LTMADS generates the directions using a random seed, while the OrthoMADS applies a deterministic sequence for generating the directions [25].

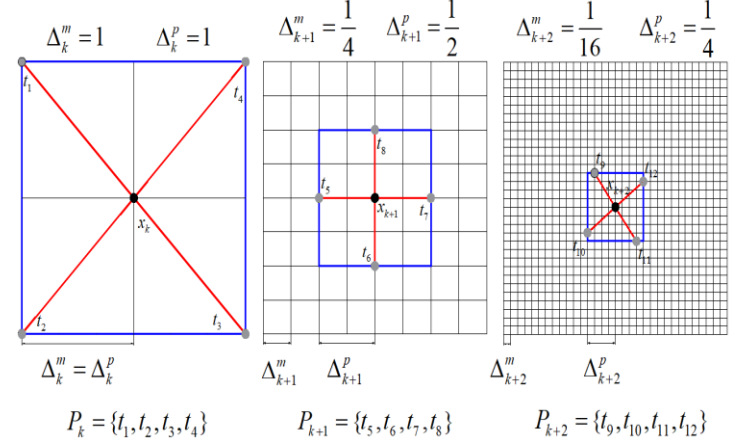


Figure 3 The principle of adaptive mesh refinement is illustrated for a two-variable case ( $D=2$ ) using three mesh configurations.  $P_k$  denotes the poll trial points. The figure is shown for the OrthoMADS subroutine with 2D directions.

## 2.6 Analysis Procedure

The vessel system variables and their respective uncertainty ranges are listed in Table 2. The sensitivity analysis necessitates that the random variables must conform to a probability distribution. As the variables were constrained with upper and lower bounds in the optimization framework, the search space resembled a Uniform distribution. Therefore, the uncertain variables were assigned with Uniform distributions with the assumption of statistical independence between the variables, for the sensitivity analysis.

Table 2 Uncertain system variables in the hydrodynamic model. The acronym of the variables is mentioned in the Nomenclature section.

$Xcg(m)$	Uniform( $lo_1 = -6.74\% Lpp$ , $up_1 = 3.82\% Lpp$ )
$Ycg(m)$	Uniform( $lo_2 = -11.9\% B$ , $up_2 = 11.9\% B$ )
$Zcg(m)$	Uniform( $lo_3 = 19.1\% T$ , $up_3 = 50.9\% T$ )
$M(kg)$	Uniform( $lo_4 = M - 5\% M$ , $up_4 = M + 5\% M$ )
$I_{44}(kgm^2)$	Uniform( $lo_5 = I_{44} - 5\% I_{44}$ , $up_5 = I_{44} + 5\% I_{44}$ )
$I_{55}(kgm^2)$	Uniform( $lo_6 = I_{55} - 5\% I_{55}$ , $up_6 = I_{55} + 5\% I_{55}$ )
$I_{66}(kgm^2)$	Uniform( $lo_7 = I_{66} - 5\% I_{66}$ , $up_7 = I_{66} + 5\% I_{66}$ )
$\beta_{33}(\frac{kg}{s})$	Uniform( $lo_8 = 0\% \beta_{33,cr}$ , $up_8 = 14\% \beta_{33,cr}$ )
$\beta_{44}(kg \frac{m^2}{s})$	Uniform( $lo_9 = 5\% \beta_{44,cr}$ , $up_9 = 35\% \beta_{44,cr}$ )
$\beta_{55}(kg \frac{m^2}{s})$	Uniform( $lo_{10} = 0\% \beta_{55,cr}$ , $up_{10} = 14\% \beta_{55,cr}$ )

$$\beta_{ff,cr} = 2\sqrt{(M_{ff} + A_{\infty,ff})C_{ff}}, ff = 3,4,5$$

The first 7 variables in Table 2 are characterized as operational-dependent parameters, whereas the remaining three variables

represent the additional viscous damping coefficients and are considered sea state-dependent. The operational-dependent parameters could not be measured accurately during the course of an operation. Additionally, the hydrodynamic analysis based on potential flow theory cannot resolve the viscous damping. Thus, these parameters were included as uncertain parameters. The acronym of the variables is presented in the Nomenclature section.

The steps involved in the practical implementation of the proposed methodology in Figure 4 are described below.

- a) The 2-dimensional ocean wave spectra, corresponding to the geographic vessel position and time, were procured from the metocean database.  $\theta_m$  was converted to Oceanographic conventions to conform with the numerical vessel response analysis.

The complete effects of each uncertain parameter on the response variation were studied using the PCE-Sobol' indices. Variables with noticeable sensitivity values were regarded as influential parameters ( $x_{in} \subset \mathbf{x}$ ), while the rest were considered as non-influential parameters ( $x_{nin} \subset \mathbf{x}$ ). The sensitivity analysis was conducted using the High-fidelity FD model (HFM). The HFM simulates the response QoI when provided with directional wave spectra,  $V_\theta, \theta_m, \mathbf{x}$  as inputs. The HFM executes every simulation by calling the Wamit hydrodynamic code. The sensitivity analysis can be performed once, prior to the start of the operation.

- b) As listed in Table 2, the influential system parameters ( $x_{in}$ ) were assigned with proper upper and lower limits. The optimization routine considers the mean value ( $x_{in}^\mu$ ) of the influential variables as initial starting points. On the other hand, a deterministic value ( $x_{nin}^\mu$ ) was accounted for the non-influential variables and applied directly in the FD analysis.

- c) A separate low-fidelity FD model (LFM) was created for performing cost-effective optimization. The LFM uses multi-dimensional interpolation on an extensive 6-dimensional vessel RAO database. The RAO database was prepared beforehand by running the Wamit code for a range of influential system variables, wave frequencies, and directions. The LFM model simulates the response QoI when provided with directional wave spectra,  $V_\theta, \theta_m, x_{in}$  as inputs.

- d) The OrthoMADS subroutine with  $D_{dir} = 2D$  directions were employed for the optimization. Further, Latin-Hypercube sampling was utilized to generate the search points in the mesh. The number of LH points for the first and each subsequent iteration were  $l_0 = 12$  and  $l_k = 12$ , respectively. Unit weight was assigned to the objective function. The optimization was conducted using a Python package that establishes

an interface to the Nonlinear Mesh Adaptive Direct Search (NOMAD) c++ library [24]. In the optimization routine, the objective function was evaluated iteratively to minimize the discrepancies between the measured and the simulated QoI. Finally, the obtained optimum parameters ( $x_{in}^*$ ) were applied in the HFM model for predicting improved responses  $(\sigma_{Z_q, HFM}^+, S_{Z_{qq}, HFM}^+)$ .

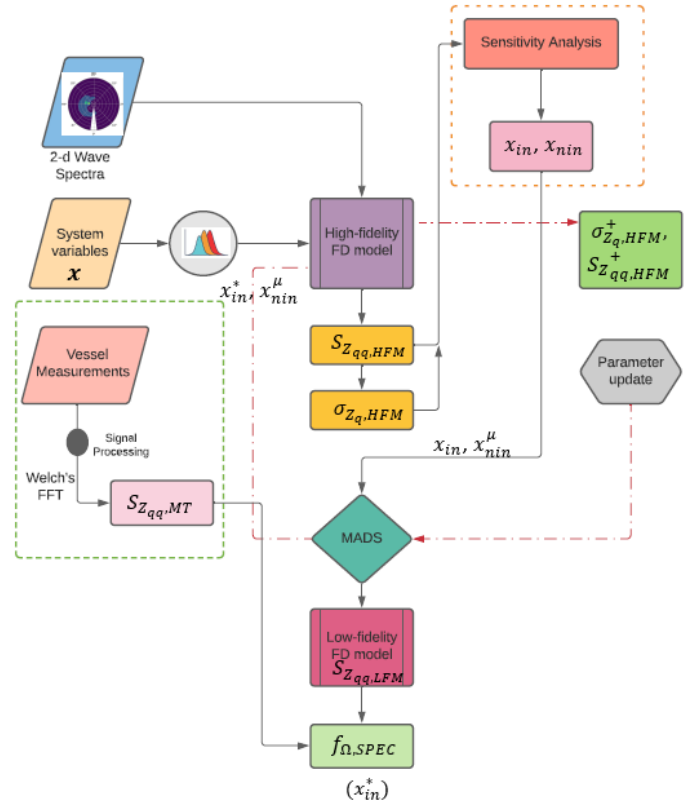


Figure 4 Flowchart showing the practical implementation of the proposed model calibration methodology.

- e) The parameters must be updated again by recursive optimization to account for changes in the vessel's operational conditions and sea states.

### 3. RESULTS AND DISCUSSIONS

#### 3.1 Sensitivity Study

The sensitivity of the Roll RMS and spectrum, due to the uncertainties in the input parameters, was evaluated considering the sea states between 07:00 – 08:00 AM. In Figure 5 a), the Roll RMS is clearly sensitive to the CoG and  $\beta_{44}$  variation. The complete effect of  $\beta_{44}$  seems to cause 51% of the total RMS variation. The CoG variables display interactive behavior and cause considerable variability to the Roll RMS. For instance,

the total effect of  $Y_{cg}$  is 24%, with the first-order/main effects constituting almost 18%, while the remaining 6% arises from the interaction of  $Y_{cg}$  with the  $X_{cg}$ (5%) and  $Z_{cg}$ (1%) parameters. The  $Z_{cg}$  and  $\beta_{44}$  parameters are also faintly interacting. The sensitivity of the complete Roll spectrum, shown in Figure 5 b), also displays similar behavior. The CoG variables and  $\beta_{44}$  are responsible for maximum variation in the wave frequency region. Specifically,  $Z_{cg}$  and  $\beta_{44}$  exerts more influence close to the Roll natural period (11.5 s). Therefore, the CoG and  $\beta_{44}$  were regarded as influential variables in the model calibration.

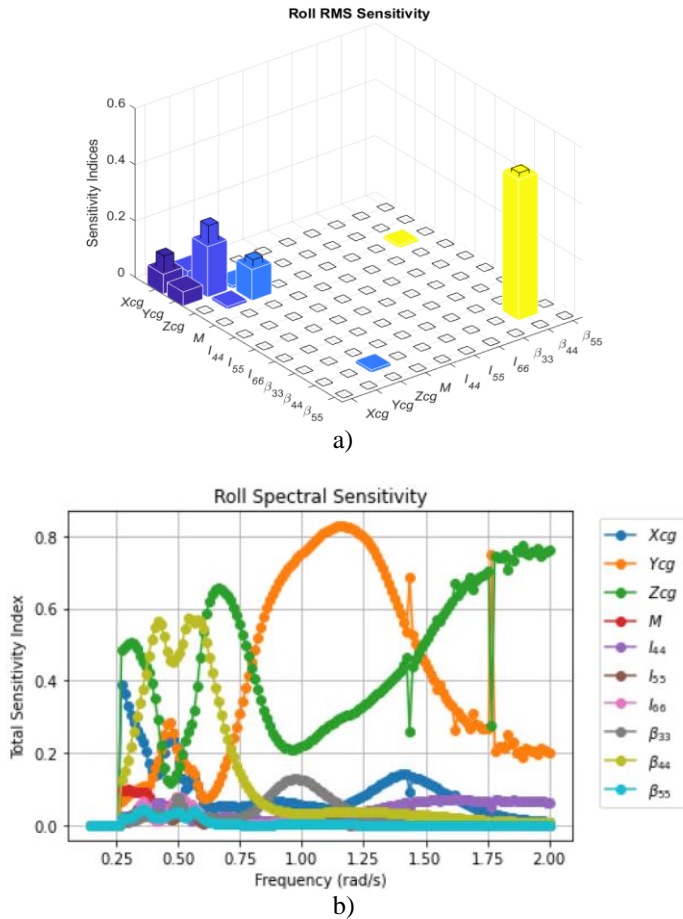


Figure 5 a) Sensitivity of the Roll RMS due to changes in the input variables. The diagonal elements denote the first-order indices, the off-diagonal elements represent the second-order indices, and the total-indices are presented on the top of the first-order indices. b) Sensitivity of the Roll spectra at each frequency.

### 3.2 Wave spectra comparisons

The effectiveness and accuracy of the numerical spectra over the parametric spectra are illustrated using Figure 6 a) and b). Using the JONSWAP formulation, the parametric spectrum was constructed by procuring the relevant sea state parameters for the wind sea and total swell from the ERA5 database. Here, the JONSWAP spectra were constructed for wind sea and swell

separately. Subsequently, the response spectra were computed individually for each sea and then combined together.

The JONSWAP formulation is affected by uncertainties related to the calculation of peak shape factors( $\gamma$ ) and peak periods( $T_p$ ). Considerable differences can be seen between the two wave spectra in Figure 6 a). There were two swell partitions at 19.00-20.00 hours; the exact energy spread of different swell partitions is present in the numeric spectrum, whereas such information is absent in the parametric spectrum.

Figure 6 b) shows the Roll responses simulated based on ECMWF and JONSWAP spectra. The ECMWF spectrum-based Roll simulation exhibit better agreement with the measured Roll response at 19:00-20:00 hours. This is especially visible at the second response peak because considerable wave energy is concentrated in the frequency regime between 0.65-0.95 rad/s. The ECMWF spectrum accounts for that spectral energy, whereas the parametric spectrum does not. Thus, the ECMWF numerical spectra were applied in the subsequent calculations.

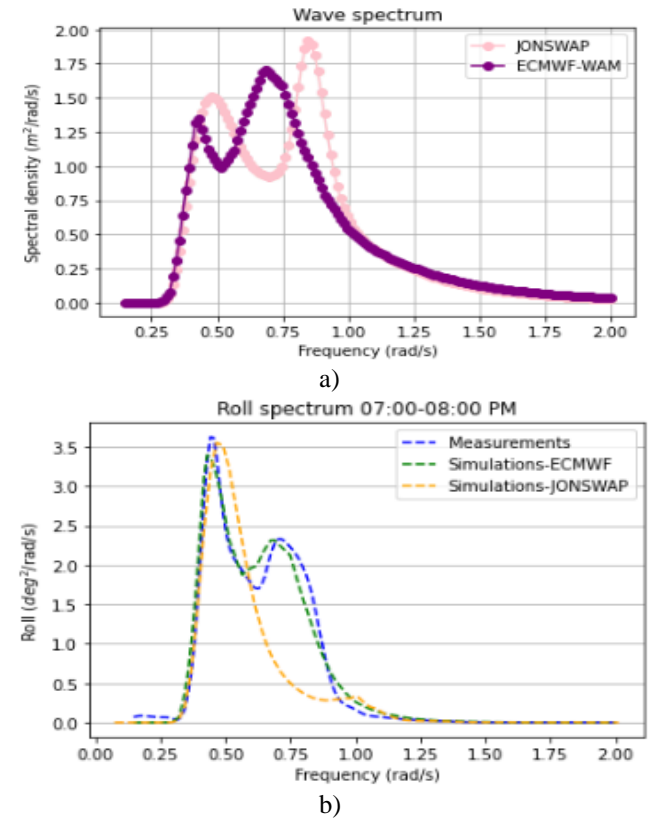


Figure 6 a) Comparison between JONSWAP and ECMWF numeric wave spectra corresponding to a sea state occurring at 19:00-20:00 hours. b) Compares the measured response spectrum with the response spectra simulated using JONSWAP and ECMWF wave spectra.

### 3.3 Model Calibration

Using measured responses between 15.00–16.00 PM, the derivative-free MADS optimization was applied to update the

influential parameters. The low-fidelity model was applied for the optimization on account of its computational efficiency. Figure 7 a) and b) clearly distinguish between the pre-and post-calibrated Roll simulations. The Roll prediction before the calibration possesses maximum deviation from the measurements. Alternatively, the post-tuned predictions show better agreement with the measurements. The influential parameters corresponding to pre-and post-calibrated cases are presented in Table 3. After the calibration, there is a 60% and 17.8% increase in  $Z_{cg}$  and  $\beta_{44}$  values, respectively, that influences the response spectrum.

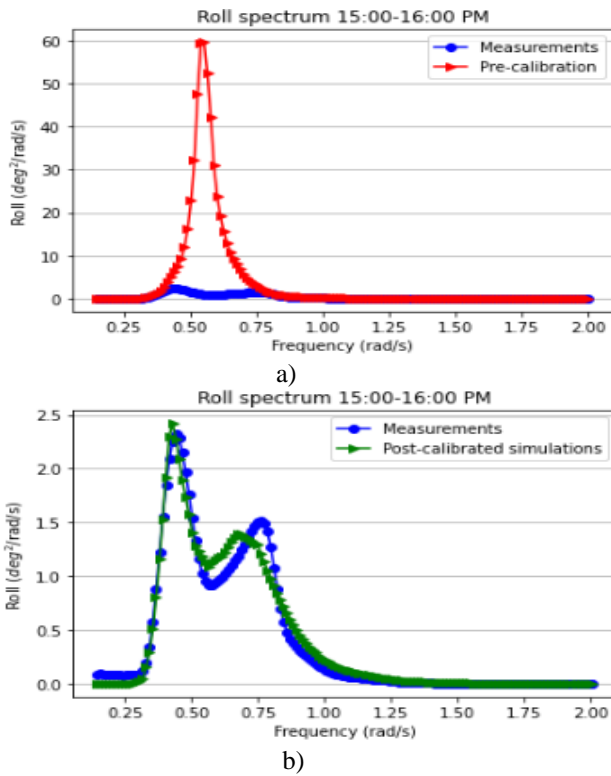


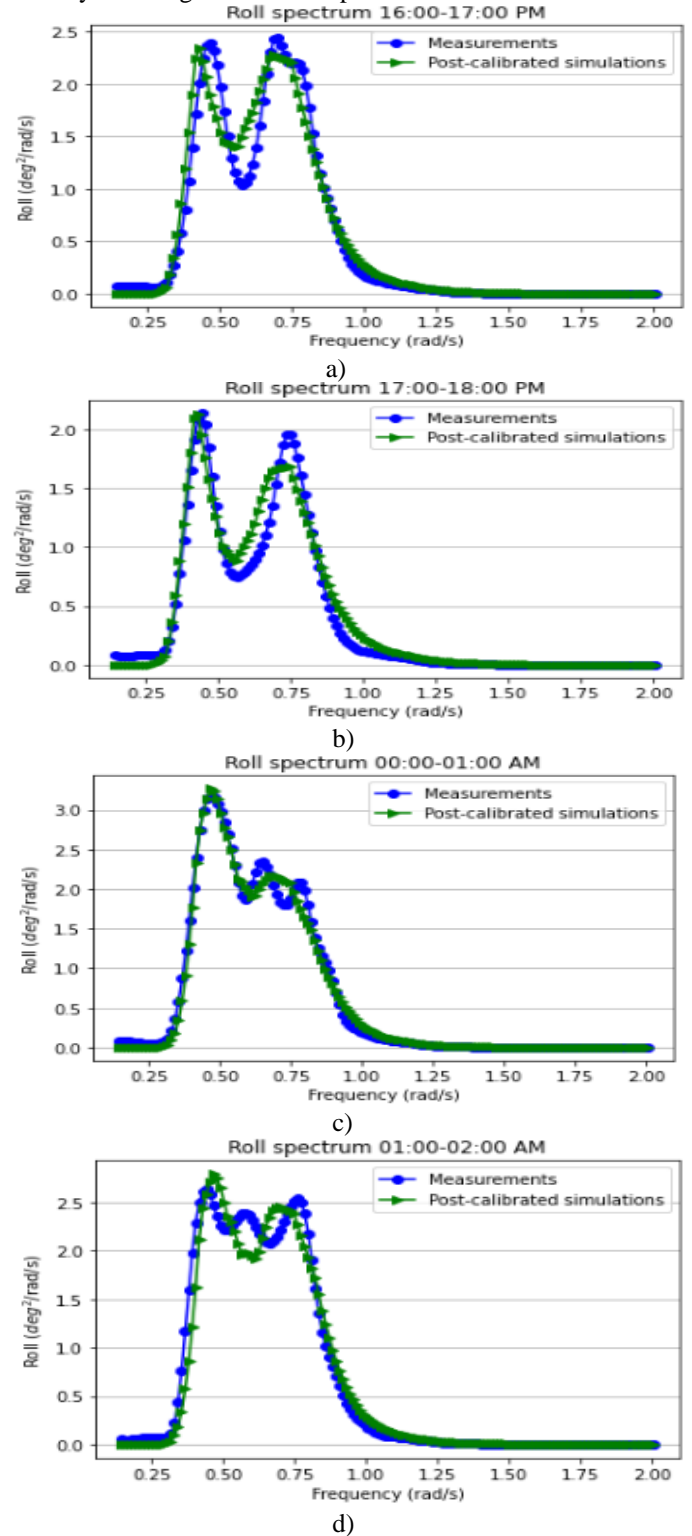
Figure 7 a) Comparison between the Roll measurements and simulations before calibration. b) Comparison between Roll measurements and Post-calibrated simulations

Table 3 Values of the influential variables before and after the calibration

	$X_{cg}(m)$	$Y_{cg}(m)$	$Z_{cg}(m)$	$\beta_{44}$
Pre-calibration	-1.3805	0.0	1.7	6% $\beta_{44,cr}$
Post-calibration	-1.2958	0.86	2.65	23.8% $\beta_{44,cr}$

Plots in Figure 8 indicate the post-calibrated Roll predictions at other sea states. Figure 8 a) and b) correspond to the first day of the operation, while the other figures correspond to the second day. In all the cases, the numerical response spectra exhibit superior agreement with the actual Rolling of the Olympic

Challenger. The first peak in Figure 8 is the Roll resonance peak, while the second peak is caused due to excitation moment. In Figure 8 a) and d), the second peak is higher than the primary resonance peak. The reason could be that the change of CoG parameters varies the natural period of Roll, thereby affecting the radiation part of the transfer function.



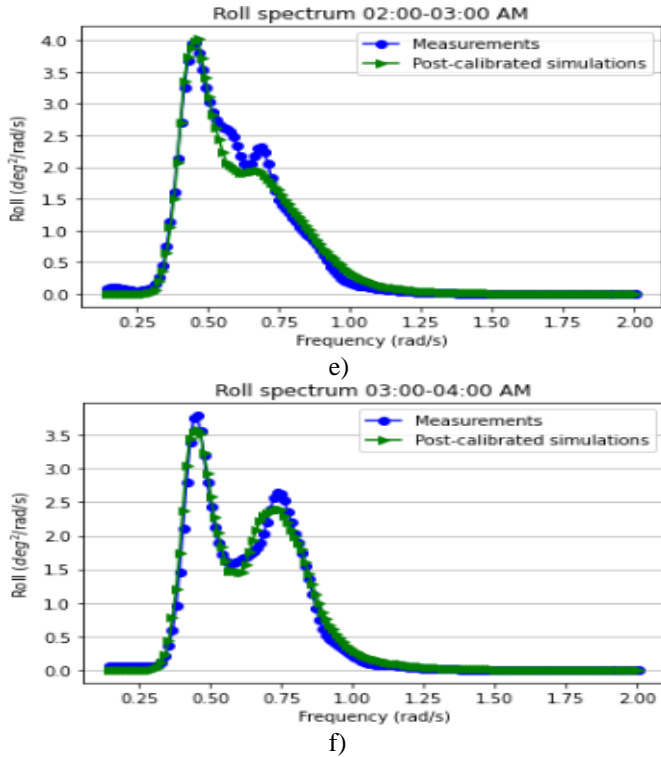


Figure 8 List of figures comparing the measured Roll spectra and post-calibrated predictions for different sea states.

### 3.4 Response Prediction Considering a Real Operational Case

The practical applicability of the calibration tool was tested considering an operational case in the month of March 2020 that spanned for 72 hours. The sea states were mostly dominated by swell conditions with 2-3 separate swell systems. The calibration was performed at the  $k-1$  step, and four different prediction cases were made for  $k+24$ ,  $k+12$ ,  $k+6$ ,  $k+3$  hours.  $k$  stands for the operational hours.

The measurements corresponding to 07:00-08:00 AM were considered in the  $0^{\text{th}}$  step for calibration. Initially, in Case 1, the calibrated variables at the  $0^{\text{th}}$  step were employed in the predictions for the next 24 hours. Then, the calibration and prediction cycle was repeated every 24 hours. In the other cases, the prediction horizon was reduced to every 12, 6, and 3 hours. The measurements and various cases of post-calibrated RMS predictions are presented in Figure 9. The post-calibrated predictions in Case 1 exhibit a noticeable deviation from 7-24 hours. The predictions improve considerably between 7-24 hours in other cases. Specifically, minor deviations from the measured RMS are seen for Case 4 compared to the other cases. The reasons could be attributed to frequent changes in the vessel operational conditions and sea states. Therefore, frequent calibration might be necessary to update the CoG parameters and  $\beta_{44}$ . On the contrary, from 50-72 hours, the post-calibrated predictions are roughly the same for all cases, indicative of minor variations in the operational conditions, roll damping coefficient, and presence of mild sea states. The

variations of the vessel parameters are further illustrated using Figure 10 a) and b).

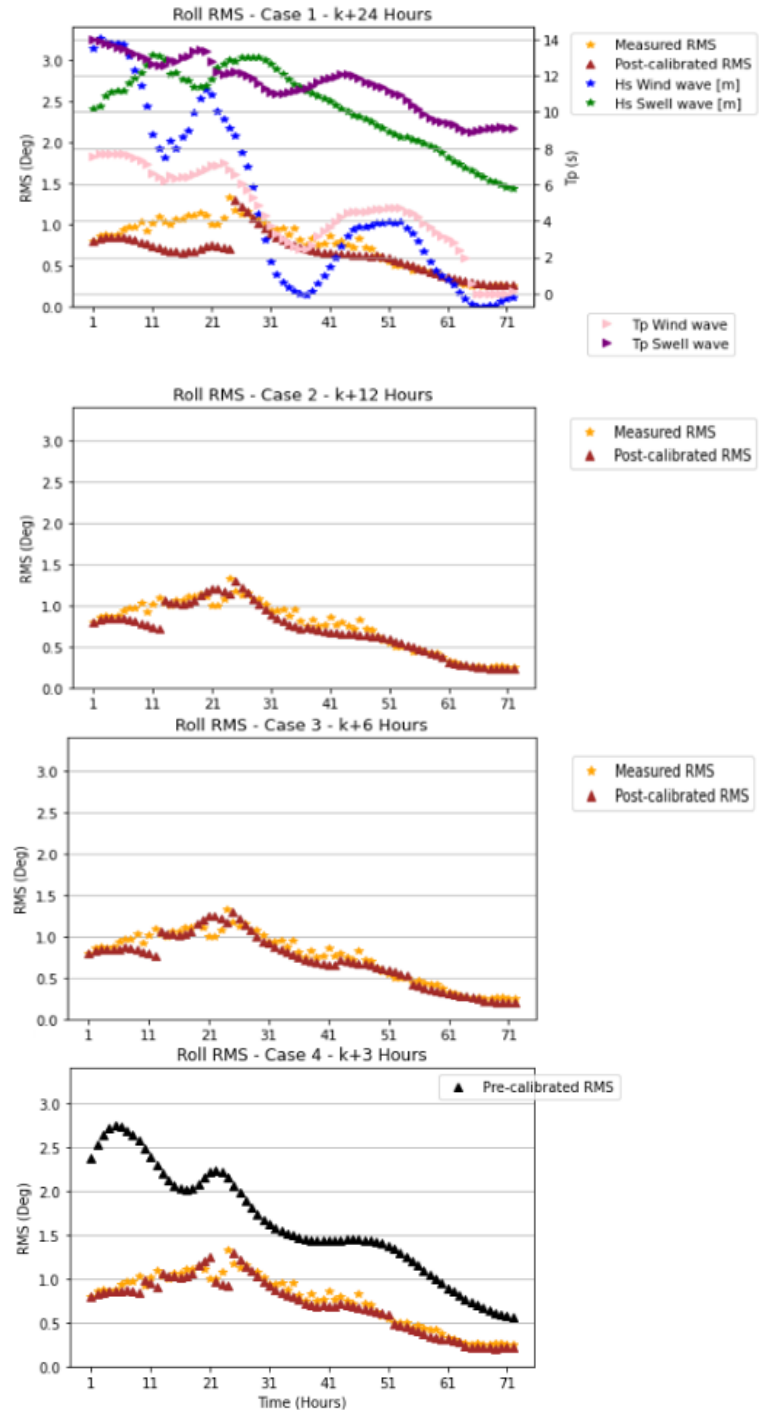


Figure 9 Recursive optimization and predictions for four cases with different time horizons. i.e., the calibration was performed at the  $k-1$  step, and the same variables were applied for predictions in  $k+24$ ,  $k+12$ ,  $k+6$ ,  $k+3$  hours.  $k$  denotes the operational hours. Case 1:  $k = 1, 25, 49$ ; Case 2:  $k = 1, 13, 25, \dots, 61$ ; Case 3:  $k = 1, 7, 13, \dots, 67$ ; Case 4:  $k = 1, 4, 7, \dots, 70$ .

In Case 4, the vessel model was updated every 3 hours during the operation. The calibrated parameters, vessel heading, and vessel's relative direction with respect to swell are presented in Figure 10, for various time instants. The calibrated system parameters include the operational-dependent CoG variables and the sea-state dependent  $\beta_{44}$ . It is seen from Figure 10 a) that the variation profile of  $Y_{cg}$  and  $Z_{cg}$  looks similar, indicating that they might be mutually interacting. These parameters vary considerably between 7-30 hours, which explains the need for frequent calibration at this time span, for better RMS prediction. Changes in vessel conditions might have triggered this variation. Specifically, between 20-30 hours, there is a peculiar coincidence between the changes in vessel heading ( $V_\theta$ ),  $\theta_R$  for swell and the variation of system parameters. This leads to the inference that the change of  $V_\theta$ , during a marine operation, may drive the CoG variation.

The profile of  $\beta_{44}$  ratio, in Figure 10 b), increases drastically after 15 hours, which could be connected with the changes in  $V_\theta$ . Suddenly, there is more than 17 % decrease in  $\beta_{44}$  after 30 hours owing to negligible wind-sea conditions. Overall, the  $\beta_{44}$  profile follows the profile of the wind-sea significant wave height in Figure 9, which is indicative of its dependent nature on sea states.

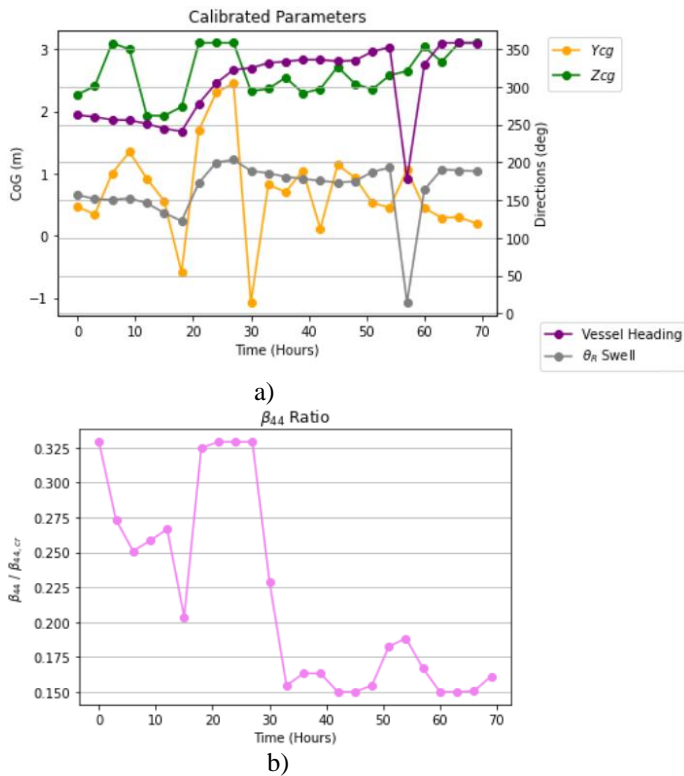


Figure 10 a)  $Y_{cg}$  and  $Z_{cg}$  parameters corresponding to Case 4 calibration are presented. Additionally, the vessel heading ( $V_\theta$ ) and vessel's relative direction ( $\theta_R$ ) with respect to incoming swell, calculated using Eq. ( 1 ), are shown. b) Ratio of linearized Roll damping coefficient to critical Roll damping for Case 4 calibration.

The quantitative error analysis based on Root Mean Squared Error (RMSE) and Mean Absolute Error (MAE) in Table 4 suggest that Case 4 has the lowest error compared to other cases. Moreover, Figure 11 shows the absolute error between the measurements and predictions at each sea state. Pre-calibrated and Case 4 predictions are considered in Figure 11. Apparently, the prediction errors are significantly minimized in Case 4. On average, there is a 91% reduction in the prediction errors compared to the case without calibration. This trend signifies the importance of performing recursive onboard model calibrations for superior response predictions.

Table 4 Root Mean Squared Errors(RMSE) and Mean Absolute Error(MAE) values for different prediction cases

		RMSE(deg)	MAE(deg)
Case 1	k+24	0.19	0.13
Case 2	k+12	0.10	0.07
Case 3	k+6	0.099	0.073
Case 4	k+3	0.096	0.070

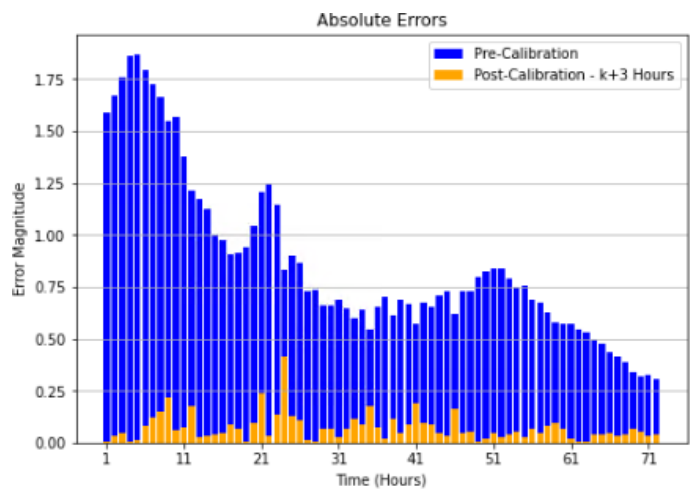


Figure 11 Error Indices to represent the absolute error between the measurements and predictions. Blue bars represent the pre-calibrated prediction errors, while the orange bars present the Case 4 prediction errors.

#### 4. CONCLUSION

A holistic model calibration framework was presented that systematically identifies the most influential variables, followed by the calibration of those variables utilizing full-scale measurements.

The sensitivity analysis based on PCE-Sobol' indices indicated that the CoG and additional viscous damping coefficient had the strongest influence on the Roll response variation. Since the CoG parameters were interacting among each other, it was considered important to tune all of them together. The changes in the mass and stiffness of the actual vessel can be accounted for in the numerical model through tuned CoG parameters. The

optimum influential parameters, obtained after calibration, resulted in response predictions that closely matched the measurements. The MADS optimization algorithm appeared to be quite effective for non-linear and noisy functions. In this study, no noise cancellation procedures were applied to the measurements since there was no information on the relevant measurement noise for the vessel response quantities. Therefore, the attributes of MADS were highly useful in this calibration work.

It was quantitatively shown that the numerical spectrum provides a more realistic representation of the wave energy, as the Roll simulations based on this spectrum produced superior results than the one based on the parametric spectrum.

Recursive optimization with shorter time horizons appeared to produce minimal prediction errors at times when there were frequent changes in vessel conditions and sea state characteristics during the operation. Therefore, it is proposed that the system parameters can be updated at least every three hours or possibly every hour during intense operational procedures.

Wamit analyses the wave-body interaction problem using potential flow theory. The potential flow solutions do not consider the viscosity of the fluid, and thereby the estimation of the viscous part of the Roll damping is significantly underpredicted. Thus, a linear additional damping coefficient was identified through calibration and added to the potential flow calculations to account for the viscous effects. Further, the model was calibrated based on FD formulations that could solve only steady-state responses and not transient effects. Therefore, the proposed framework cannot calibrate the numerical model when transient effects are present in the signal.

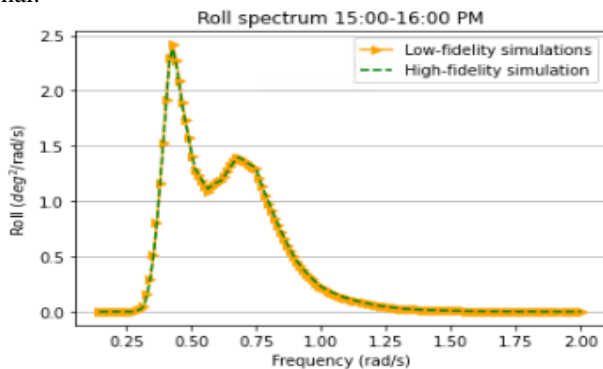


Figure 12 Compares the HFM and LFM simulation results during 15:00 -16:00 PM

The low-fidelity model was utilized inside the optimization routine. Though uncertainties might be associated with the interpolations applied in the LFM, it offers cost-effective optimization, thereby saving tremendous computational time. It is postulated that the discrepancies between the HFM and LFM-based Roll responses may be inconsequential. Thus, the

associated uncertainty due to interpolations can be ignored. To support the argument, the result of an analysis is presented in Figure 12, which compares the HFM and LFM simulations.

The methods to address the uncertainties in the system variables were described in this paper, but it neglects the uncertainties in the numerical wave prediction. The proposed methodology employs numerical spectra derived from the ERA5 reanalysis database, which are less uncertain than forecasts. So, the methodology must be extended to include forecasted spectra along with the wave forecasts uncertainty.

## ACKNOWLEDGEMENTS

This work was made possible through the Centre for Research-based Innovation MOVE, financially supported by the Research Council of Norway, NFR project no. 237929 and the consortium partners, <http://www.ntnu.edu/move>. The author would like to express gratitude and appreciation to Olympic Subsea ASA, involved in the SFI-MOVE consortium, for sharing technical details and permitting to use the data. Wim Lavrijzen, AIDE-QC, Lawrence Berkely National Laboratory, is sincerely thanked for providing the Python wheels for Nomad 4 C++ library.

## REFERENCES

- [1] GL Noble Denton, "0001/ND GENERAL GUIDELINES FOR MARINE PROJECTS," DNV GL, 2015.
- [2] NORSOK STANDARDS, "Common Requirements MARINE OPERATIONS," NORSOK Standardisation Work Group, January 1995.
- [3] W. I. G. Acero, "Assessment of marine operations for offshore wind turbine installation with emphasis on response-based operational limits," Department of Marine Technology, Norwegian University of Science and Technology, Trondheim, 2016.
- [4] G. F. Clauss and T. Riekert, "Operational limitations of Offshore Crane Vessels," in *22nd Offshore Technology Conference*, Houston, 1990.
- [5] DNV GL, "Recommended practice DNV-RP-C205 Environmental Conditions and Environmental Loads," DNV, 2010.
- [6] Coastal Engineering Research Center, "Directional wave spectra using cosine squared and cosine 2S spreading functions," Vicksburg, 1985.
- [7] THE WAMDI GROUP, "The WAM Model - A Third Generation Ocean Wave Prediction Model," *American Meteorological Society*, pp. 1775-1810, 1988.
- [8] H. L. Tolman, B. Balasubramanian, L. D. Burroughs, D. V. Chalikov, Y. Y. Chao, H. S. Chen and V. M. Gerald, "Development and Implementation of Wind-Generated Ocean Surface Wave Models at NCEP," *American Meteorological Society*, pp. 311-333, 2002.

- [9] B. Sudret, "Global sensitivity analysis using polynomial chaos expansions," *Reliability Engineering and System Safety*, pp. 964-979, 2007.
- [10] G. Blatman, "Adaptive sparse polynomial chaos expansions for uncertainty propagation and sensitivity analysis," Institut Francais de Mecanique Avancee et Universite Blaise Pascal, 2009.
- [11] G. Deman, K. Konakli, B. Sudret, J. Kerrou, P. Perrochet and H. Benabderrahmane, "Using sparse polynomial chaos expansions for the global sensitivity analysis of groundwater lifetime expectancy in a multi-layered hydrogeological model," *Reliability Engineering and System Safety*, no. 147, pp. 156-169, 2016.
- [12] C. V. Mai, "Polynomial chaos expansions for uncertain dynamical systems - Application in earthquake engineering," ETHZ, Zurich, 2016.
- [13] G. Radhakrishnan, X. Han, S. Sævik, Z. Gao and B. J. Leira, "System Uncertainty Effects on the Wave Frequency Response of Floating Vessel Based on Polynomial Chaos Expansion, OMAE2021-62542," in *Proceedings of the ASME 2021 40th International Conference on Ocean, Offshore and Arctic Engineering*, Virtual, Online, 2021.
- [14] X. Han, B. J. Leira, S. Sævik and K. E. Kaasen, "Validation of vessel seakeeping model tuning algorithm based on measurements at model scale," *Marine Structures*, p. In press, 2021.
- [15] K. E. Kaasen, "Automatic Estimation of Parameters in Numerical Vessel Models from Laboratory Tests," SINTEF Ocean AS, Trondheim, 2019.
- [16] D. Skandali, "Identification of response amplitude operators for ships based on full scale measurements," TUDelft and Marine Contractors, Delft, 2015.
- [17] ECMWF, "ERA 5: Data Documentation," 09 July 2020. [Online]. Available: <https://confluence.ecmwf.int/display/CKB/ERA5>. [Accessed 13 July 2020].
- [18] G. Komen, S. Hasselmann and K. Hasselmann, "On the Existence of a Fully Developed Wind-Sea Spectrum," *Journal of Physical Oceanography*, pp. 1271-1285, 1984.
- [19] WAMIT INC, "WAMIT, The state of the art in wave interaction analysis," Massachusetts Institute of Technology, Chestnut Hill, MA, 2014.
- [20] P. D. Welch, "The Use of Fast Fourier Transform for the Estimation of Power Spectra: A Method Based on Time Averaging Over Short, Modified Periodograms," *IEEE Transactions on Audio and ElectroAcoustics*, pp. 70-73, 1967.
- [21] A. Saltelli, M. Ratto, T. Andres, F. Campolongo, J. Cariboni, D. Gatelli and S. T. M. Saisana, *Global Sensitivity Analysis. The Primer*, Chichester; West Sussex: John Wiley & Sons, Ltd, 2008.
- [22] J. Charles Audet & J.E. Dennis, "Mesh Adaptive Direct Search Algorithms for Constrained Optimization," *SIAM Journal of Optimization*, vol. 18, no. 4, pp. 188-217, 2008.
- [23] S. L. Digabel, "NOMAD: Nonlinear Optimization with the MADS Algorithm," *ACM Transactions on Mathematical Software*, pp. 1-15, 2011.
- [24] C. Audet and J. Dennis, "Mesh adaptive direct search algorithms for constrained optimization," *SIAM Journal on Optimization*, pp. 1-26, 2006.
- [25] M. A. Abramson, C. Audet, J. E. Dennis and S. L. Digabel, "OrthoMADS: a deterministic MADS instance with orthogonal directions," *SIAM Journal on Optimization*, vol. 20, pp. 948-966, 2009.
- [26] W. Lavrijsen, "Scikit-Quant," 2021.